CHEMISTRY OF MATERIALS

Article

pubs.acs.org/cm

# Dibenzoquinquethiophene- and Dibenzosexithiophene-Based Hole-Transporting Materials for Perovskite Solar Cells

Javier Urieta-Mora,[†,‡] Iwan Zimmermann,[⊥,‡] Juan Aragó,[§] Agustín Molina-Ontoria,*[,∥] Enrique Ortí,*[,§] Nazario Martín,*[,†,∥] and Mohammad Khaja Nazeeruddin*[,⊥]

[†]Departamento Química Orgánica, Facultad C. C. Químicas, Universidad Complutense de Madrid, Av. Complutense s/n, 28040 Madrid, Spain

[⊥]Group for Molecular Engineering of Functional Materials, EPFL VALAIS, CH-1951 Sion, Switzerland

[§]Instituto de Ciencia Molecular, Universidad de Valencia, Catedrático José Beltrán 2, 46980 Paterna, Spain

[∥]IMDEA-Nanociencia, C/Faraday 9, Ciudad Universitaria de Cantoblanco, 28049 Madrid, Spain

Supporting Information

**ABSTRACT:** Fused oligothiophene-based $\pi$-conjugated organic derivatives have been widely used in electronic devices. In particular, two-dimensional (2D) heteroarenes offer the possibility of broadening the scope by extending the $\pi$-conjugated framework, which endows enhanced charge transport properties due to the potential intermolecular $\pi-\pi$ stacking. Here, the synthesis and characterization of two new small-molecule hole-transporting materials (HTMs) for perovskite solar cells (PSCs) are reported. The newly custom-made compounds are based on dibenzoquinquethiophene (DBQT) and dibenzosexithiophene (DBST) cores, which are covalently linked to triphenylamine moieties to successfully afford the four-armed tetrakistriphenylamine (TTPA) derivatives **TTPA−DBQT** and **TTPA−DBST**. The combination of these novel central scaffolds with the electron-donor TTPA units bestow the resulting HTMs with the appropriate energy levels and, therefore, good electronic contact with the perovskite for extracting the hole efficiently. **TTPA−DBQT** surpasses **TTPA−DBST** not only in terms of conductivity but also in light-to-energy conversion efficiency using conventional mesoscopic n−i−p perovskite devices, 18.1% and 14.3%, respectively. These results were systematically compared with the benchmark HTM, 2,2′,7,7′-tetrakis(*N*,*N*-di-*p*-methoxyphenylamine)-9,9′-*spiro*bifluorene (spiro-OMeTAD). Additionally, scanning electron microscopy (SEM) hints that **TTPA−DBQT** forms high quality and fully homogeneous films, whereas **TTPA−DBST** leads to the formation of thinner films with pinholes, which explains its lower fill factor despite its better hole-extraction properties owing to its more planar $\pi$-extended scaffold.

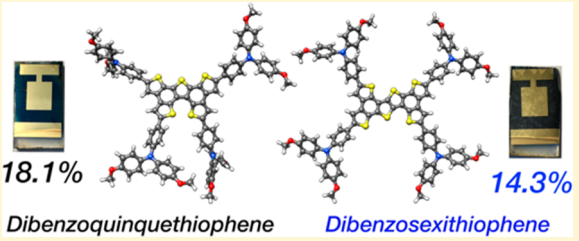


## INTRODUCTION

Pressed by the drastic reduction of fossil fuels, harvesting energy by alternative sources has become one of the most important challenges that our society will face in the coming years. In this regard, the immense amount of energy that we receive from our sun can be considered as the main source of power for our future society. Nowadays, solar cell devices based on silicon are leading the photovoltaic sector, transforming 25% of the incident sunlight into electricity. Notwithstanding, these high-power conversion efficiency (PCE) values for silicon solar cells, the high production cost of these cells has encouraged the quest for new low-cost and efficient photovoltaic devices.

Since the advent of the hybrid inorganic−organic perovskite solar cells (PSCs) reported by Miyasaka and co-workers as sensitizers for dye-sensitized solar cells (DSSCs),[1] PSCs have emerged as a promising technology for light harvesting in the future, displaying efficiencies over 22.7%.[2] Hybrid perovskites usually contain small organic cations, such as methylammonium (MA) or formamidinium (FA), and lead halides (e.g., $MAPbI_3$) and exhibit extraordinary properties such as high charge-carrier mobilities,[3−5] tunable band gap energy,[6] long free charge-carrier diffusion lengths,[7−9] wide light absorption,[10] and solution-processed fabrication. Perovskites allow the preparation of different device architectures depending on the charge selective contacts used to sandwich the perovskite. To date, the most featured and efficient devices are based on mesoporous structures, where the perovskite is infiltrated in a dense mesoporous scaffold of $TiO_2$ (mp-$TiO_2$), in combination with organic hole-transporting materials (HTMs), the most widely used HTM being the 2,2′,7,7′-tetrakis(*N*,*N*-di-*p*-methoxyphenylamine)-9,9′-*spiro*bifluorene (spiro-OMeTAD) compound.[11,12]

Despite its great performance, spiro-OMeTAD presents a relatively high commercial price owing to its tough (Grignard

Special Issue: Jean-Luc Bredas Festschrift

Received: September 20, 2018
Revised: December 5, 2018
Published: December 7, 2018





DOI: 10.1021/acs.chemmater.8b04003
Chem. Mater. XXXX, XXX, XXX−XXX

reaction, bromination reaction, and a Hartwig−Buchwald C−N coupling) and low-yield (less than 40%) synthetic preparation and costly purification.[13] These drawbacks have promoted the design and synthesis of alternative new HTMs. In this regard, different types of organic HTMs, with and without the spiro-motif,[14−17] from classical polymers or oligomers to small $\pi$-conjugated structures, have been investigated in PSCs.[18−20]

Flat, sulfur-containing, polycyclic aromatic structures have been extensively used in the literature for field-effect transistors OFETs[21] and photovoltaic applications[22−24] because they give rise to planar structures and the sulfur-rich arenes introduce extra intermolecular interactions ($\pi-\pi$, S···S) that affect the packing of the derivatives (face-to-edge to face-to-face), thus enhancing the hole-carrier mobilities. These chalcogenide-rich polycyclic aromatics have been recently described as promising scaffolds for building novel HTMs for PSCs due to their good conductivity and excellent performance.[25−27] This behavior is beautifully exemplified by anthra[1,2-*b*:4,3-*b*′:5,6-*b*″:8,7-*b*‴]-tetrathiophene (ATT) derivatives introduced by Zimmermann et al. as HTMs, where $\pi-\pi$ stacking is surmised as one of the main reasons for their enhanced conductivity and efficiency in PSCs.[28]

Inspired by these findings, we present herein two new HTMs, in which the $\pi$-conjugation of the central core has been systematically modulated. Particularly important in this design is to control the molecular packing by introducing highly planar structures, which is an important parameter for enhancing carrier mobilities. Promoting the intermolecular assembly by $\pi-\pi$ and S···S interactions serves as a powerful paradigm for the design of more efficient HTMs. On this basis, we have synthesized two novel sulfur-rich cores, dibenzoquinquethiophene (DBQT) and dibenzosexithiophene (DBST), to which four triphenylamine (TPA) units are attached at the $\alpha$-positon of the four terminal thiophene rings giving rise to the tetrakistriphenylamine (TTPA) derivatives sketched in Chart 1. The new derivatives **TTPA−DBQT** and **TTPA−DBST** not only exhibit a proper energy alignment of the highest-occupied molecular orbital (HOMO), which ensures efficient hole injection to the perovskite, but also good conductivity values. Power conversion efficiencies of up to 18.1% are derived from mesoscopic perovskite solar cells using the new HTMs and the compositionally engineered perovskite $[FAPbI_3]_{0.85}[MAPbBr_3]_{0.15}$, which is comparable to the PCE value obtained for the state-of-the-art spiro-OMeTAD.

**Chart 1. Chemical Structures of the Two New HTMs**

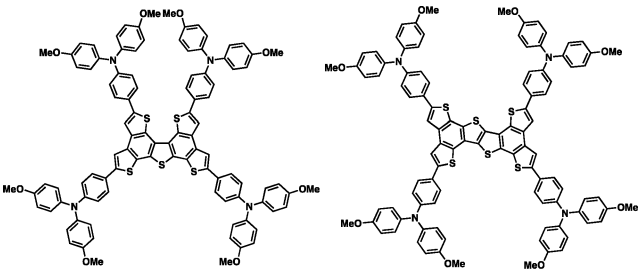


## ■ RESULTS AND DISCUSSION

**Synthesis.** The new HTMs were built up following similar synthetic pathways as described in Scheme 1 (see the Supporting Information for experimental details). The DBQT and DBST cores were prepared by a 4-fold Pd-mediated Stille cross-coupling reaction or Pd-mediated Suzuki coupling reaction between commercially available tetrabromo derivatives and 2-(tributyl)stannylthiophene or 2-thienylboronic acid affording compounds **1** and **4**, respectively, which were then converted into the tetrabromo derivatives **2** and **5** by a regioselective bromination reaction in $\alpha$-position. Utilizing a $FeCl_3$-mediated oxidative C−C coupling protocol, $\pi$-extended derivatives **3** and **6** were cleanly obtained in excellent yields. Finally, a 4-fold Suzuki cross coupling reaction with *p*-methoxytriphenylamine successfully furnished **TTPA−DBQT** and **TTPA−DBST** as orange solids, in 74% and 68% yields, respectively.

**Scheme 1. Synthetic Procedure for the Preparation of DBQT (3) and DBST (6) Cores**

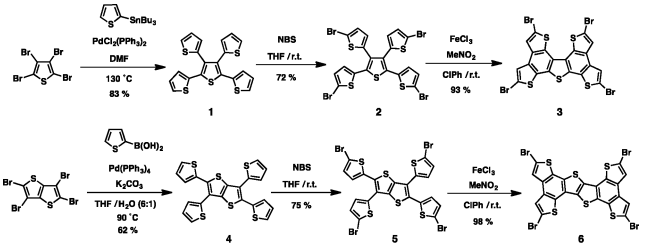

Complete structural characterization of the designed **TTPA−DBQT** and **TTPA−DBST** HTMs and the corresponding intermediates was conducted by using standard spectroscopic techniques such as $^1$H NMR, $^{13}$C NMR, FTIR, and UV−visible (for more details, see the Supporting Information). Mass spectrometry (MALDI-TOF) confirmed the presence of **TTPA−DBQT** and **TTPA−DBST** with molecular ion peaks [M]+ at 1620.4273 and 1676.3986 *m*/*z*, respectively.

**Theoretical Calculations.** To gain insight into the structural and electronic properties of the **TTPA−DBQT** and **TTPA−DBST** compounds, density functional theory (DFT) calculations were performed at the B3LYP/6-31G** level in the presence of the solvent ($CH_2Cl_2$). Their respective cores (DBQT and DBST), the pendant triphenylamine TPA moiety, and the reference spiro-OMeTAD compound were also computed for comparison purposes (see the Supporting Information for full computational details).

Figure S1 displays the most representative bond length values calculated at the B3LYP/6-31G** level for the DBQT and DBST cores and the **TTPA−DBQT** and **TTPA−DBST** HTMs. The DBQT and DBST cores can be visualized as formed by two benzotrithiophene (BTT) units. In the case of DBQT, the two BTT units share the central thiophene ring and define a conjugated all-*syn* 2,2′,5′,2″-terthiophene with the external thiophene rings. Due to the condensation with the adjacent benzenes, the central thiophene ring exhibits longer carbon−carbon (C−C) bonds (1.417−1.479 Å) than the external thiophene rings (1.372−1.432 Å), the latter being more similar to those found for nonfused thiophene oligomers.[29] In the case of the DBST core, the two BTT units define a central fused bithienyl unit with C−C bond lengths more similar to those expected for fused oligothiophenes,[30] which is conjugated with two external thiophene rings in a *syn* 2,2′-disposition. Therefore, both the DBQT and the DBST core present an effective conjugation path between the thiophene rings connected by the 2,2′-positions. For the


DOI: 10.1021/acs.chemmater.8b04003
Chem. Mater. XXXX, XXX, XXX−XXX

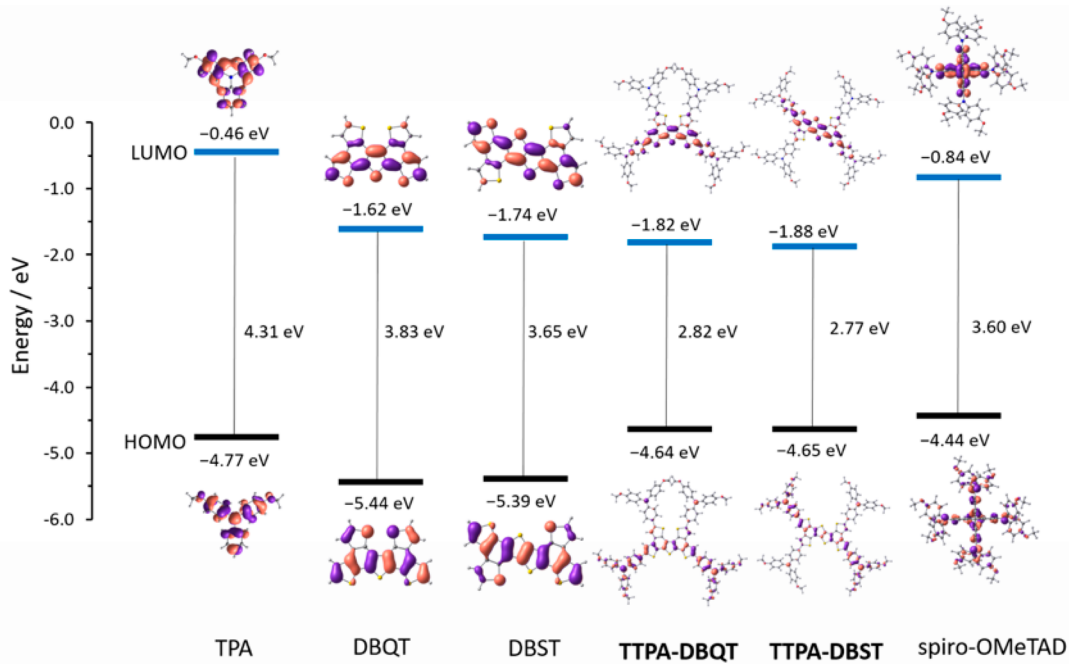


**Figure 1.** Energy diagram displaying the frontier molecular orbitals computed at the B3LYP/6-31G** level for the TPA unit, the DBQT and DBST cores, the **TTPA−DBQT** and **TTPA−DBST** HTMs, and the spiro-OMeTAD reference compound.

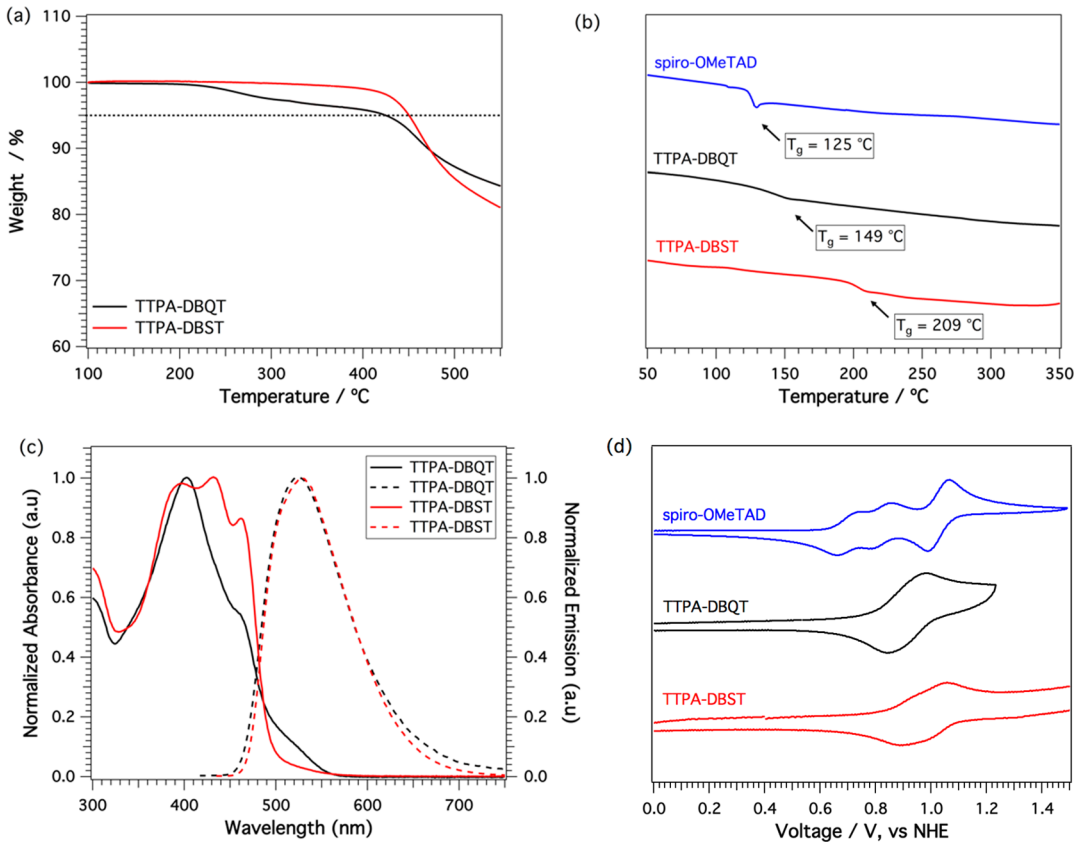


**Figure 2.** (a) Thermogravimetric analysis curves recorded for **TTPA−DBQT** and **TTPA−DBST** under nitrogen at 10 °C $min^{-1}$ of heating rate. (b) Differential scanning calorimetry of spiro-OMeTAD, **TTPA−DBQT**, and **TTPA−DBST** under nitrogen at a heating rate of 20 °C $min^{-1}$ (second cycle). (c) UV−vis absorption (solid line) and fluorescence emission spectra (dashed line) of **TTPA−DBQT** and **TTPA−DBST** derivatives in $CH_2Cl_2$, measured at ambient temperature. (d) Cyclic voltammograms of **TTPA−DBQT** and **TTPA−DBST** derivatives in $TBAPF_6$/$CH_2Cl_2$ at a scan rate of 100 mV $s^{-1}$.

HTMs, the insertion of the four TPA units hardly causes any substantial change in the bond distances of the conjugated core, with the exception of the terminal C−C and carbon−sulfur bonds to which the TPA units are linked (Figure S1). It



DOI: 10.1021/acs.chemmater.8b04003
Chem. Mater. XXXX, XXX, XXX−XXX

Table 1. Thermal, Electrochemical, and Photophysical Properties of TTPA−DBQT, TTPA−DBST, and spiro-OMeTAD

| HTM | $T_{dec}$ [°C][a] | $T_g$ [°C][b] | $E^{ox}_{1/2}$ [V][c] | $E_{HOMO}$ [eV][d] | $\lambda_{max,abs}$ [nm][e] | $\lambda_{max,em}$ [nm][e] | $E^{0-0}$ [eV][f] | $E_{LUMO}$ [eV][g] |
|---|---|---|---|---|---|---|---|---|
| **TTPA−DBQT** | 423 | 149 | 0.88 | −5.32 | 403 | 522 | 2.60 | −2.72 |
| **TTPA−DBST** | 450 | 209 | 0.93 | −5.37 | 431 | 528 | 2.57 | −2.80 |
| spiro-OMeTAD | 449 | 125 | 0.72 | −5.16 | 386 | 319 | 3.05 | −2.11 |

[a]Decomposition temperature determined from TGA (5% weight loss under a $N_2$ atmosphere). [b]Determined from the second cycle of the DSC under a $N_2$ atmosphere. [c]Determined from CV measurements vs normal hydrogen electrode (NHE). [d]$E_{HOMO}$ is estimated in eV by $E_{HOMO} = -4.44$ eV $- E^{ox}_{1/2}$. [e]$\lambda_{max}$ of absorption and emission was measured in $CH_2Cl_2$ solutions. [f]$E^{0-0}$ was determined at the intersection of normalized absorption and emission spectra. [g]$E_{LUMO}$ was estimated by $E_{LUMO} = E_{HOMO} + E^{0-0}$.

should be emphasized that both HTMs preserve the planarity of the polycyclic core (Figure S2).

Figure 1 displays the frontier molecular orbitals calculated for TPA, the DBQT and DBST cores, the **TTPA−DBQT** and **TTPA−DBST** HTMs, and the spiro-OMeTAD reference compound. The highest-occupied molecular orbital (HOMO) of the DBQT and DBST cores, computed at −5.44 and −5.39 eV, respectively, are significantly lower in energy than the HOMO of TPA (−4.77 eV) in accord with their weaker electron-donor character. In line with the molecular structure, the HOMOs of DBQT and DBST mainly spread over the most effective conjugated path and their topology resembles those obtained for oligothiophene derivatives.[31,32] The HOMOs of the four-armed DBQT and DBST derivatives are significantly destabilized (−4.64 and −4.65 eV, respectively) as a consequence of the incorporation of the TPA moieties. This destabilization, which implies an enhancement of the electron-donor character, shifts up the HOMO levels close to that computed for the reference spiro-OMeTAD (−4.44 eV). Note that the HOMO of both **TTPA−DBQT** and **TTPA−DBST** spreads not only over the respective cores but also over the TPA moieties connected to the thiophene rings where the conjugation is more effective. It should be noted that a significant charge transfer occurs from the peripheral TPA groups to the sulfur-rich central cores, which hold a total net charge of −0.55e and −0.56e for **TTPA−DBQT** and **TTPA−DBST**, respectively. The obtained electronic structure of the **TTPA−DBQT** and **TTPA−DBST** HTMs is therefore significantly polarized.

**Thermal and Optical Properties.** Thermogravimetric analysis (TGA) of the new HTMs revealed their good thermal stability (5% weight loss under $N_2$ atmosphere) up to 450 °C for **TTPA−DBST** and 423 °C for **TTPA−DBQT**, which demonstrates the robustness of these HTMs (Figure 2a). The latter exhibits a slight weight loss (3%) in the range of 150−350 °C, which is attributed to traces of solvent molecules trapped after purification of the material. Detailed thermal features are collected in Table 1. The thermal behavior of **TTPA−DBQT** and **TTPA−DSQT** was inspected by means of differential scanning calorimetry (DSC) (Figure 2b). Glass transition temperatures ($T_g$) were determined from the second heating cycle. Both molecules exhibit reduced tendency to crystallize with a glass transition temperature of 149 °C for **TTPA−DBQT** and 209 °C for **TTPA−DBST**, which confirms their amorphous behavior. $T_g$ is indeed higher for the two new HTM derivatives in comparison with that for spiro-OMeTAD ($T_g$ = 125 °C), which is attributed to improved molecular packing, indicating higher stability in the amorphous state.

The absorption and emission spectra of the new HTMs are shown in Figure 2c, and the corresponding data are collected in Table 1. In $CH_2Cl_2$, **TTPA−DBQT** and **TTPA−DBST** display an intense absorption in the UV and at short wavelengths of the visible region (<500 nm), in sharp contrast with the limited absorbance of spiro-OMeTAD in the visible. The absorption maxima ($\lambda_{max,abs}$) for **TTPA−DBQT** and **TTPA−DBST** are centered at 403 nm ($\varepsilon = 1.2 \times 10^4$ M cm$^{-1}$) and 431 nm ($\varepsilon = 1.4 \times 10^4$ M cm$^{-1}$), respectively. The broader and red-shifted absorption of **TTPA−DBST** compared with **TTPA−DBQT** is ascribed to the more extended $\pi$-conjugation of the central DBST fragment and is in agreement with the lower HOMO−LUMO gap predicted for **TTPA−DBST** (Figure 1). B3LYP/6-31G** calculations of the lowest-lying singlet excited electronic states ascribe the broad experimental absorption band recorded for **TTPA−DBQT** to six intense $S_0 \rightarrow S_n$ ($n$ = 1−6) electronic transitions computed in the 429−505 nm range. For **TTPA−DBST**, three intense electronic transitions ($S_0 \rightarrow S_1$, $S_0 \rightarrow S_2$, and $S_0 \rightarrow S_6$) computed in the 420−513 nm range seem to be responsible for the more structured experimental band. The intense electronic transitions in both HTMs are of $\pi-\pi^*$ nature and imply one-electron promotions from the HOMO − 3, HOMO − 2, HOMO − 1, and HOMO to the LUMO, LUMO + 1, and LUMO + 2, which reside on both the core and the peripheral TPA groups (see Table S1 and Figure S3). The emission maximum of **TTPA−DBQT** is located at 522 nm, whereas that of **TTPA−DBST** displays a slight bathochromic shift peaking at 528 nm. Furthermore, it is observed that the intersection of the absorption and emission occurs at 477 and 481 nm for **TTPA−DBQT** and **TTPA−DBST**, respectively, which corresponds to analogous band gap energy values of 2.60 and 2.57 eV, respectively.

**Electrochemical Properties.** The redox properties of the novel HTM were investigated by cyclic voltammetry (CV) in $TBAPF_6/CH_2Cl_2$ at a scan rate of 100 mV s$^{-1}$ (Figure 2d). For better understanding, spiro-OMeTAD was also measured under the same experimental conditions. The oxidation potentials and the HOMO energies are summarized in Table 1. The cyclic voltammogram of **TTPA−DBQT** shows one oxidation wave with $E_{1/2}$ values of 0.88 V vs NHE. The broad shape of the oxidation wave seems to result from the overlapping of two oxidation waves that can be tentatively assigned to consecutive very close oxidation processes where four electrons are successively extracted from the TPA units. However, the **TTPA−DBST** exhibits two waves at 0.93 and 1.02 V vs NHE, respectively. The different central moieties do not have a strong impact on the electrochemical properties. The HOMO energies derived from the first oxidation potential for **TTPA−DBQT** and **TTPA−DBST** are −5.32 and −5.37 eV, respectively, which are ∼0.2 eV lower than the energy obtained for spiro-OMeTAD (−5.16 eV) and in very good accord with the theoretical values estimated for the isolated molecules (Figure 1). Therefore, an efficient hole extraction from the perovskites to the HTMs is ensured due to the


DOI: 10.1021/acs.chemmater.8b04003
Chem. Mater. XXXX, XXX, XXX−XXX

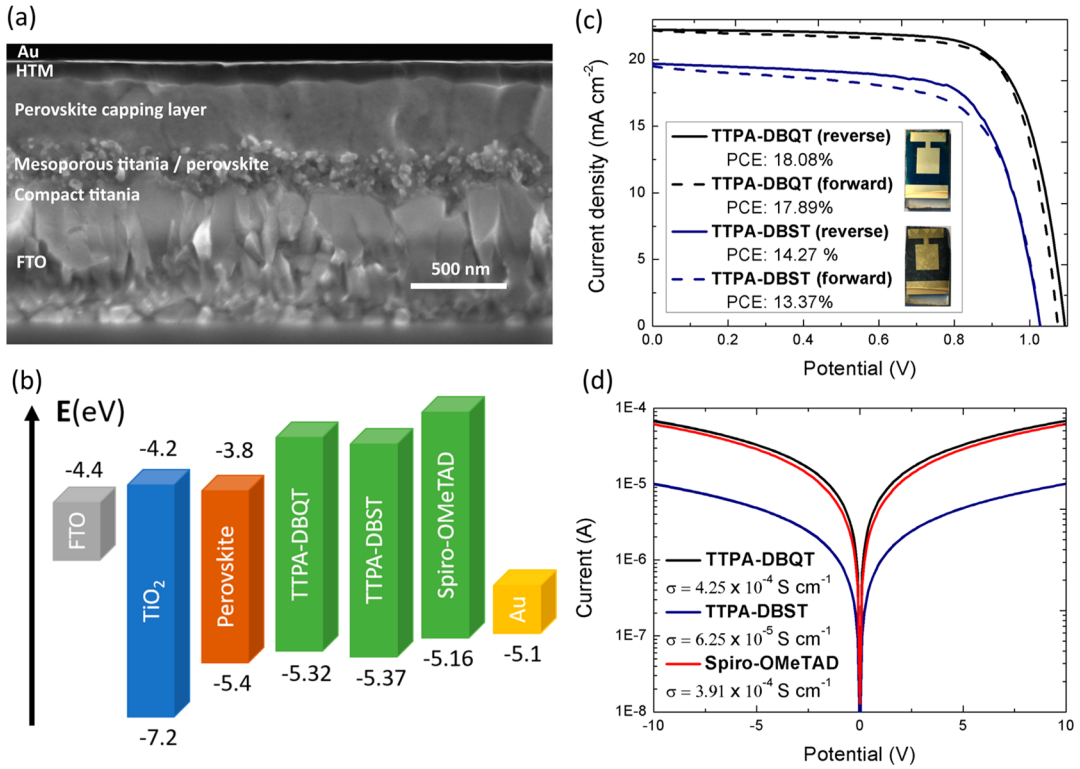


**Figure 3.** Device characterization: (a) SEM cross-section image of a PSC having **TTPA−DBQT** as HTM. (b) Energy diagram of the different components used in the PSC. (c) Solar cell efficiency of the champion devices measured under 1.5G simulated sunlight. (d) Conductivity of the different HTMs measured on substrates having interdigitating gold electrodes.

excellent band alignment with the valence band edge of the perovskite (ca. −5.4 eV).

To gain a better understanding of the oxidation processes, the oxidized species (up to the tetracation) of **TTPA−DBQT** and **TTPA−DBST** were calculated at the B3LYP/6-31G** level in $CH_2Cl_2$. Table S1 gathers the charges accumulated by the constituting fragments (central cores and TPA units) as oxidation takes place. In line with the topology of the HOMO of **TTPA−DBQT** and **TTPA−DBST** (Figure 1), the charge for the radical cation species is mainly extracted from the DBQT and DBST cores (ca. 0.30e) and the TPA units linked to the terminal 2-positions of the thiophene rings (ca. 0.27e) that define the most effective conjugation pathway within the cores. Upon further oxidation, the charge is steadily drawn from the four TPA units. For the tetracation, they hold a similar charge of ca. +1.0e and the cores lose the excess of electron density shown in the neutral state (Table S1). It should be noted that, for both **TTPA−DBQT** and **TTPA−DBST**, the ionization energies (IEs) required for passing from the neutral molecule to the cation (IE1), from the cation to the dication (IE2), from the dication to the trication (IE3), and from the trication to the tetracation (IE4) are predicted to have relatively close values. For instance, the IE1, IE2, IE3, and IE4 values for **TTPA−DBQT** were calculated to be 4.55, 4.79, 5.00, and 5.09 eV, respectively, and very similar values (4.57, 4.79, 4.95, and 5.05 eV, respectively) were obtained for **TTPA−DBST**. The largest difference in IE values is between IE1 and IE2 (0.24 and 0.22 eV for **TTPA−DBQT** and **TTPA−DBST**, respectively). The closeness of the IE values explains the electrochemical behavior found for **TTPA−DBQT** and **TTPA−DBST** showing a broad four-electron oxidation wave (Figure 2d).

Hole reorganization energies ($\lambda$) were calculated at the B3LYP/6-31G** level in gas phase to evaluate the capability of the **TTPA−DBQT** and **TTPA−DBST** compounds as HTMs (see the planar core). Both **TTPA−DBQT** and **TTPA−DBST** exhibit low reorganization energy similar to those found for other excellent *p*-type semiconducting organic materials[33,34] and in the same range as that obtained for the reference spiro-OMeTAD (0.139 eV).[28] Therefore, **TTPA−DBQT** and **TTPA−DBST** present a great potential as hole-transporting materials for PSC devices owing to its small $\lambda$ value and the appropriate energy level alignment with the valence band edge of the perovskite.

**Photovoltaics Properties.** Solution-processed perovskite solar cells were prepared to investigate the performance of the novel HTMs compared to the widely used reference compound spiro-OMeTAD. The photovoltaic devices were fabricated following a standard procedure for the well-studied n−i−p configuration with a mixed ion perovskite $(FAPbI_3)_{0.85}(MAPbBr_3)_{0.15}$ as the active light-harvesting material, previously reported to yield high efficiencies.[35] The solar cells consist of a stack of thin film layers deposited onto a FTO substrate. Titania was used as the electron-selective contact sandwiching the light-absorbing perovskite material with the HTM. The perovskite layer was obtained using a one-step spin-coating process using chlorobenzene as quenching solvent as previously described by Jeon et al.[36] The HTMs were applied on top of the perovskite film by spin-coating their corresponding solutions in chlorobenzene for **TTPA−DBQT** and spiro-OMeTAD and tetrachloroethane for **TTPA−DBST**, respectively. Tetrachloroethane was used instead of chlorobenzene due to the low solubility of **TTPA−DBST**. Tert-butylpyridine (*t*-BP), tris(2-(1*H*-pyrazol-1-yl)-4-*tert*-


DOI: 10.1021/acs.chemmater.8b04003
Chem. Mater. XXXX, XXX, XXX−XXX

butylpyridine)cobalt(III) (FK209), and tris(bis-(trifluoromethylsulfonyl)imide) (Li-TFSI) were added as additives. Further details on the device fabrication can be found in the Supporting Information. The individual thin film layers of a PSC device can be observed from the cross-sectional scanning electron microscopy (SEM) image shown in Figure 3a where **TTPA−DBQT** was applied as the HTM. Energy levels of the different HTMs as well as other components in the PSC can be found in Figure 3b.

Device efficiencies were investigated under AM 1.5G (100 mW $cm^{-2}$) simulated sunlight. The $J-V$ curves of the champion devices using **TTPA−DBQT** and **TTPA−DBST** are shown in Figure 3c, and the corresponding reference using spiro-OMeTAD can be found in Figure S5. Devices fabricated with **TTPA−DBQT** were shown to perform superior to **TTPA−DBST**-based PSCs (Table 2). Efficiencies up to 18.08% (open circuit voltage ($V_{oc}$) = 1.09 V; short circuit current ($J_{sc}$) = 22.2 mA $cm^{-2}$; fill factor (FF) = 74.4%) could be obtained using **TTPA−DBQT**, whereas for **TTPA−DBST** the champion device exhibited an efficiency of 14.27% ($V_{oc}$ = 1.03 V; $J_{sc}$ = 19.7 mA $cm^{-2}$; FF = 70.6%) measuring in the reverse scan direction. Almost negligible hysteresis was observed for **TTPA−DBQT** with a performance difference between reverse and forward scan of only 1%, whereas for **TTPA−DBST** the difference in performance was around 6%. The performance for the solar cell based on spiro-OMeTAD was very close to that obtained for **TTPA−DBQT** with an efficiency of 17.96% ($V_{oc}$ = 1.09 V; $J_{sc}$ = 22.6 mA $cm^{-2}$; FF = 73.1%). The lower performance of **TTPA−DBST** stemmed from its low solubility and therefore complicated processability. Tetrachloroethane was used as an alternative solvent which lead to the formation of a very thin HTM layer of only 20−50 nm as can be seen from the SEM image (Figure S7). Furthermore, the thin film turned out to be less uniform than for **TTPA−DBQT** looking at the finished devices displayed as an inset in Figure 3c. This indicates the formation of pinholes within the HTM layer, which would explain the reduced $V_{oc}$ and $J_{sc}$ of the **TTPA−DBST** devices due to direct contact of the gold layer with the perovskite material. The $J_{sc}$ obtained from the $J-V$ measurements and the integrated current densities from the external quantum efficiencies (EQEs) are in good agreement, within 5% (Figure S6).

**Table 2. Device Performance of the New TTPA−DBQT and TTPA−DBST HTMs Compared with the Reference spiro-OMeTAD**

| HTM | scan direction | $V_{oc}$ [V] | $J_{sc}$ [mA $cm^{-2}$] | fill factor [%] | PCE [%] |
|---|---|---|---|---|---|
| **TTPA−DBQT** | forward | 1.07 | 22.20 | 75.0 | 17.89 |
| | reverse | 1.09 | 22.23 | 74.4 | 18.08 |
| **TTPA−DBST** | forward | 1.03 | 19.51 | 66.7 | 13.37 |
| | reverse | 1.03 | 19.68 | 70.6 | 14.27 |
| spiro-OMeTAD | forward | 1.07 | 22.54 | 72.7 | 17.56 |
| | reverse | 1.08 | 22.60 | 73.1 | 17.96 |

**Charge Transfer Properties and Conductivity.** To have a better understanding of the charge extraction processes, steady-state photoluminescence (PL) was recorded. As shown in Figure S8, the pristine perovskite film exhibit a strong PL signal steaming from the radiative recombination of the photogenerated charge carriers. A significantly decreased PL signal is observed upon deposition of the HTMs on top of the perovskite layer, provoked by an efficient quenching of the photogenerated charge carriers. This suggests a good hole extraction for both **TTPA−DBST** and **TTPA−DBQT** comparable to spiro-OMeTAD, which is in agreement with the well-aligned HOMO energy levels as discussed above. The more planar molecular structure predicted for **TTPA−DBST** (Figure S2) results in a more efficient hole extraction than for **TTPA−DBQT**, which may be attributed to better contact between the perovskite and the HTM. Intriguingly, the improved charge extraction capability of **TTPA−DBST** does not translate into a better photovoltaic performance than **TTPA−DBQT**. As mentioned before, the poor solubility of the former resulted in nonhomogeneous and poor film-forming ability, as observed in the cross-sectional image shown in Figure S7. The surface coverage of perovskite layer by **TTPA−DBST** is not uniformly distributed, leading to the formation of pinholes, which affects significantly not only the charge collection but also the device performance.

Further justification for the PSC efficiencies obtained with the different HTMs could be obtained by conductivity measurements (Figure 3d). The conductivity of the different molecules was measured on substrates having interdigitating gold electrodes with a channel length of 2.5 $\mu$m. The same concentration as for the device preparation was used by adding 6% of FK-209 as dopant. The highest conductivity was observed for **TTPA−DBQT** ($4.25 \times 10^{-4}$ S·$cm^{-1}$), slightly higher than that of spiro-OMeTAD ($3.91 \times 10^{-4}$ S·$cm^{-1}$). The conductivity of **TTPA−DBST** ($6.25 \times 10^{-5}$ S·$cm^{-1}$), on the other hand, was around 1 order of magnitude lower, which further corroborates its low $J_{sc}$, poor FF, and therefore lower PCEs compared with **TTPA−DBQT**.

## CONCLUSIONS

In summary, we report the syntheses and study the properties of two new custom-made HTMs based on innovative two-dimensional heteroarenes as central scaffolds for highly efficient PSCs. These new derivatives comprise dibenzoquinquethiophene (DBQT) and dibenzosexithiophene (DBST), which are covalently linked to four *p*-methoxytriphenylamine units. A detailed characterization and comparison of the thermal and optoelectronic properties was conducted. Both HTMs are thermally stable with glass transition temperatures higher than 100 °C and exhibit very similar HOMO and LUMO energy levels, which ensure a good alignment with the valence band edge of the perovskite. Upon assessing both HTMs in mesoporous devices, remarkable light-to-energy conversion efficiencies of 18.1% and 14.27% are measured for **TTPA−DBQT** and **TTPA−DBST**, respectively, which are similar to the efficiency obtained for the widely used spiro-OMeTAD (17.96%). **TTPA−DBQT** shows not only the highest performance with no hysteresis but also better solubility (processability) and conductivity values, which are 1 order of magnitude higher than those measured for **TTPA−DBST**. The lower solubility of **TTPA−DBST** in chlorobenzene leads to poor coverage of the perovskite surface and to the formation of pinholes, which significantly affect the device performance. Good processability of the HTM from solution is a very important parameter for reaching high performing devices. Therefore, a compromise between the extended molecular structure and the solubility must be taken into account. Attaching longer alkyl chains can be envisioned as a complementary strategy to overcome this drawback, but it may affect other properties such as conductivity. Finally, promoting


DOI: 10.1021/acs.chemmater.8b04003
Chem. Mater. XXXX, XXX, XXX−XXX

the intermolecular assembly by $\pi-\pi$ and S···S interactions using fused oligothiophene-based $\pi$-conjugated systems as a central core serves as an excellent approach for designing highly efficient HTMs.

## ■ ASSOCIATED CONTENT

### Supporting Information

The Supporting Information is available free of charge on the ACS Publications website at DOI: 10.1021/acs.chemmater.8b04003.

General materials and methods; synthetic procedures and characterization, such as $^{1}$H NMR, $^{13}$C NMR, and mass spectrometry (MALDI-TOF); computational details; device fabrication and characterization, such as hysteresis, EQE measurements, SEM, and steady-state photoluminescence (PDF)

## ■ AUTHOR INFORMATION


### Corresponding Authors

*Homepage: http://www.nazariomartingroup.com/. E-mail: nazmar@ucm.es.

*E-mail: mdkhaja.nazeeruddin@epfl.ch.

*E-mail: enrique.orti@uv.es.

*E-mail: agustin.molina@imdea.org.

### ORCID

Juan Aragó: 0000-0002-0415-9946

Enrique Ortí: 0000-0001-9544-8286

Nazario Martín: 0000-0002-5355-1477

Mohammad Khaja Nazeeruddin: 0000-0001-5955-4786

### Author Contributions

‡J.U.-M. and I.W. contributed equally to this work.


### Notes

The authors declare no competing financial interest.

## ■ ACKNOWLEDGMENTS

We thank the Swiss National Funds for Scientific Research contract number 200020L_172929/1, Project "Tailored Design and in-depth understanding of perovskite solar materials using in-house developed 3D/4D nanoscale ion-beam analysis". Borun New Material Technology generously supplied the high-quality spiro-OMeTAD. The authors also thank the European Research Council (ERC-320441-Chirallcarbon), the Spanish Ministry of Economy and Competitiveness MINECO (Project Nos. CTQ2014-52045-R, CTQ2015-71154-P, CTQ2015-71936-REDT, and CTQ2016-81911-REDT, Unidad de Excelencia Severo Ochoa SEV-2016-0686, and Unidad de Excelencia María de Maeztu MDM-2015-0538), the CAM (FOTOCARBON Project No. S2013/MIT-2841), the Generalitat Valenciana (No. PROMETEO/2016/135), and European Feder funds (No. CTQ2015-71154-P). J.A. is grateful to MINECO for a "JdC-incorporación" postdoctoral fellowship (No. IJCI-2015-26154).

## ■ REFERENCES


(1) Kojima, A.; Teshima, K.; Shirai, Y.; Miyasaka, T. Organometal Halide Perovskites as Visible-Light Sensitizers for Photovoltaic Cells. *J. Am. Chem. Soc.* **2009**, *131*, 6050−6051.

(2) National Renewable Energy Laboratory. http://www.nrel.gov/ncpv/images/efficiency_chart.jpg (accessed June 20, 2016).

(3) Ponseca, C. S.; Savenije, T. J.; Abdellah, M.; Zheng, K.; Yartsev, A.; Pascher, T.; Harlang, T.; Chabera, P.; Pullerits, T.; Stepanov, A.; Wolf, J.-P.; Sundström, V. Organometal Halide Perovskite Solar Cell Materials Rationalized: Ultrafast Charge Generation, High and Microsecond-Long Balanced Mobilities, and Slow Recombination. *J. Am. Chem. Soc.* **2014**, *136*, 5189−5192.

(4) Savenije, T. J.; Ponseca, C. S.; Kunneman, L.; Abdellah, M.; Zheng, K.; Tian, Y.; Zhu, Q.; Canton, S. E.; Scheblykin, I. G.; Pullerits, T.; Yartsev, A.; Sundström, V. Thermally Activated Exciton Dissociation and Recombination Control the Carrier Dynamics in Organometal Halide Perovskite. *J. Phys. Chem. Lett.* **2014**, *5*, 2189−2194.

(5) Oga, H.; Saeki, A.; Ogomi, Y.; Hayase, S.; Seki, S. Improved Understanding of the Electronic and Energetic Landscapes of Perovskite Solar Cells: High Local Charge Carrier Mobility, Reduced Recombination, and Extremely Shallow Traps. *J. Am. Chem. Soc.* **2014**, *136*, 13818−13825.

(6) Eperon, G. E.; Stranks, S. D.; Menelaou, C.; Johnston, M. B.; Herz, L. M.; Snaith, H. J. Formamidinium lead trihalide: a broadly tunable perovskite for efficient planar heterojunction solar cells. *Energy Environ. Sci.* **2014**, *7*, 982−988.

(7) Stranks, S. D.; Eperon, G. E.; Grancini, G.; Menelaou, C.; Alcocer, M. J. P.; Leijtens, T.; Herz, L. M.; Petrozza, A.; Snaith, H. J. Electron-Hole Diffusion Lengths Exceeding 1 Micrometer in an Organometal Trihalide Perovskite Absorber. *Science* **2013**, *342*, 341−344.

(8) Dong, Q.; Fang, Y.; Shao, Y.; Mulligan, P.; Qiu, J.; Cao, L.; Huang, J. Electron-hole diffusion lengths > 175 $\mu$m in solution-grown $CH_3NH_3PbI_3$ single crystals. *Science* **2015**, *347*, 967.

(9) Xing, G.; Mathews, N.; Sun, S.; Lim, S. S.; Lam, Y. M.; Grätzel, M.; Mhaisalkar, S.; Sum, T. C. Long-Range Balanced Electron- and Hole-Transport Lengths in Organic-Inorganic $CH_3NH_3PbI_3$. *Science* **2013**, *342*, 344−347.

(10) Kazim, S.; Nazeeruddin, M. K.; Grätzel, M.; Ahmad, S. Perovskite as Light Harvester: A Game Changer in Photovoltaics. *Angew. Chem., Int. Ed.* **2014**, *53*, 2812−2824.

(11) Saliba, M.; Matsui, T.; Seo, J.-Y.; Domanski, K.; Correa-Baena, J.-P.; Nazeeruddin, M. K.; Zakeeruddin, S. M.; Tress, W.; Abate, A.; Hagfeldt, A.; Gratzel, M. Cesium-containing triple cation perovskite solar cells: improved stability, reproducibility and high efficiency. *Energy Environ. Sci.* **2016**, *9*, 1989−1997.

(12) Bi, D.; Tress, W.; Dar, M. I.; Gao, P.; Luo, J.; Renevier, C.; Schenk, K.; Abate, A.; Giordano, F.; Correa Baena, J.-P.; Decoppet, J.-D.; Zakeeruddin, S. M.; Nazeeruddin, M. K.; Grätzel, M.; Hagfeldt, A. Efficient luminescent solar cells based on tailored mixed-cation perovskites. *Sci. Adv.* **2016**, *2*, No. e1501170.

(13) Zhang, J.; Hua, Y.; Xu, B.; Yang, L.; Liu, P.; Johansson, M. B.; Vlachopoulos, N.; Kloo, L.; Boschloo, G.; Johansson, E. M. J.; Sun, L.; Hagfeldt, A. The Role of 3D Molecular Structural Control in New Hole Transport Materials Outperforming Spiro-OMeTAD in Perovskite Solar Cells. *Adv. Energy Mater.* **2016**, *6*, 1601062.

(14) Saliba, M.; Orlandi, S.; Matsui, T.; Aghazada, S.; Cavazzini, M.; Correa-Baena, J.-P.; Gao, P.; Scopelliti, R.; Mosconi, E.; Dahmen, K.-H.; De Angelis, F.; Abate, A.; Hagfeldt, A.; Pozzi, G.; Graetzel, M.; Nazeeruddin, M. K. A molecularly engineered hole-transporting material for efficient perovskite solar cells. *Nat. Energy* **2016**, *1*, 15017.

(15) Bi, D.; Xu, B.; Gao, P.; Sun, L.; Grätzel, M.; Hagfeldt, A. Facile synthesized organic hole transporting material for perovskite solar cell with efficiency of 19.8%. *Nano Energy* **2016**, *23*, 138−144.

(16) Malinauskas, T.; Saliba, M.; Matsui, T.; Daskeviciene, M.; Urnikaite, S.; Gratia, P.; Send, R.; Wonneberger, H.; Bruder, I.; Graetzel, M.; Getautis, V.; Nazeeruddin, M. K. Branched methoxydiphenylamine-substituted fluorene derivatives as hole transporting materials for high-performance perovskite solar cells. *Energy Environ. Sci.* **2016**, *9*, 1681−1686.

(17) Cabau, L.; Garcia-Benito, I.; Molina-Ontoria, A.; Montcada, N. F.; Martin, N.; Vidal-Ferran, A.; Palomares, E. Diarylamino-substituted tetraarylethene (TAE) as an efficient and robust hole transport material for 11% methyl ammonium lead iodide perovskite solar cells. *Chem. Commun.* **2015**, *51*, 13980−13982.

(18) Cho, I.; Jeon, N. J.; Kwon, O. K.; Kim, D. W.; Jung, E. H.; Noh, J. H.; Seo, J.; Seok, S. I.; Park, S. Y. Indolo[3,2-b]indole-based




DOI: 10.1021/acs.chemmater.8b04003
*Chem. Mater.* XXXX, XXX, XXX−XXX

crystalline hole-transporting material for highly efficient perovskite solar cells. *Chem. Sci.* **2017**, *8*, 734−741.
(19) Chen, C.; Cheng, M.; Liu, P.; Gao, J.; Kloo, L.; Sun, L. Application of benzodithiophene based A−D−A structured materials in efficient perovskite solar cells and organic solar cells. *Nano Energy* **2016**, *23*, 40−49.
(20) Bi, D.; Mishra, A.; Gao, P.; Franckevičius, M.; Steck, C.; Zakeeruddin, S. M.; Nazeeruddin, M. K.; Bäuerle, P.; Grätzel, M.; Hagfeldt, A. High-Efficiency Perovskite Solar Cells Employing a S,N-Heteropentacene-based D−A Hole-Transport Material. *ChemSusChem* **2016**, *9*, 433−438.
(21) Wang, C.; Dong, H.; Hu, W.; Liu, Y.; Zhu, D. Semiconducting π-Conjugated Systems in Field-Effect Transistors: A Material Odyssey of Organic Electronics. *Chem. Rev.* **2012**, *112*, 2208−2267.
(22) Dang, D.; Fan, J.; Wang, X.; Xiao, M.; Shi, J.; Zhou, P.; Duan, X.; Lei, G.; Liu, Y.; Zhu, W. Influence of the fused hetero-aromatic centers on molecular conformation and photovoltaic performance of solution-processed organic solar cells. *New J. Chem.* **2015**, *39*, 2224−2232.
(23) Dang, D.; Xiao, M.; Zhou, P.; Zhong, J.; Fan, J.; Su, N.; Xiong, W.; Yang, C.; Wang, Q.; Wang, Y.; Pei, Y.; Yang, R.; Zhu, W. Tuning the Isomeric Fused Heteroaromatic Core of Small Donor−Acceptor Molecules to Alter Their Crystalline Nature and Enhance Photovoltaic Performance. *Eur. J. Org. Chem.* **2015**, *2015*, 820−827.
(24) Dang, D.; Zhou, P.; Zhong, J.; Fan, J.; Wang, Z.; Wang, Y.; Pei, Y.; Bao, X.; Yang, R.; Hu, W.; Zhu, W. Novel wide band-gap polymer utilizing fused hetero-aromatic unit for efficient polymer solar cells and field-effect transistors. *Polymer* **2014**, *55*, 6708−6716.
(25) Garcia-Benito, I.; Zimmermann, I.; Urieta-Mora, J.; Arago, J.; Molina-Ontoria, A.; Orti, E.; Martin, N.; Nazeeruddin, M. K. Isomerism effect on the photovoltaic properties of benzotrithiophene-based hole-transporting materials. *J. Mater. Chem. A* **2017**, *5*, 8317−8324.
(26) Molina-Ontoria, A.; Zimmermann, I.; Garcia-Benito, I.; Gratia, P.; Roldán-Carmona, C.; Aghazada, S.; Graetzel, M.; Nazeeruddin, M. K.; Martín, N. Benzotrithiophene-Based Hole-Transporting Materials for 18.2% Perovskite Solar Cells. *Angew. Chem., Int. Ed.* **2016**, *55*, 6270−6274.
(27) García-Benito, I.; Zimmermann, I.; Urieta-Mora, J.; Aragó, J.; Calbo, J.; Perles, J.; Serrano, A.; Molina-Ontoria, A.; Ortí, E.; Martín, N.; Nazeeruddin, M. K. Heteroatom Effect on Star-Shaped Hole-Transporting Materials for Perovskite Solar Cells. *Adv. Funct. Mater.* **2018**, *28*, 1801734.
(28) Zimmermann, I.; Urieta-Mora, J.; Gratia, P.; Aragó, J.; Grancini, G.; Molina-Ontoria, A.; Ortí, E.; Martín, N.; Nazeeruddin, M. K. High-Efficiency Perovskite Solar Cells Using Molecularly Engineered, Thiophene-Rich, Hole-Transporting Materials: Influence of Alkyl Chain Length on Power Conversion Efficiency. *Adv. Energy Mater.* **2017**, *7*, 1601674.
(29) Aragó, J.; Ponce Ortiz, R.; Nieto-Ortega, B.; Hernández, V.; Casado, J.; Facchetti, A.; Marks, T. J.; Viruela, P. M.; Ortí, E.; López Navarrete, J. T. Carbonyl-Functionalized Quaterthiophenes: A Study of the Vibrational Raman and Electronic Absorption/Emission Properties Guided by Theoretical Calculations. *ChemPhysChem* **2012**, *13*, 168−176.
(30) Arago, J.; Viruela, P. M.; Gierschner, J.; Orti, E.; Milian-Medina, B. Oligothienoacenes versus oligothiophenes: impact of ring fusion on the optical properties. *Phys. Chem. Chem. Phys.* **2011**, *13*, 1457−1465.
(31) Aragó, J.; Viruela, P. M.; Ortí, E.; Malavé Osuna, R.; Vercelli, B.; Zotti, G.; Hernández, V.; López Navarrete, J. T.; Henssler, J. T.; Matzger, A. J.; Suzuki, Y.; Yamaguchi, S. Neutral and Oxidized Triisopropylsilyl End-Capped Oligothienoacenes: A Combined Electrochemical, Spectroscopic, and Theoretical Study. *Chem. - Eur. J.* **2010**, *16*, 5481−5491.
(32) Malavé Osuna, R.; Hernández, V.; López Navarrete, J. T.; Aragó, J.; Viruela, P. M.; Ortí, E.; Suzuki, Y.; Yamaguchi, S.; Henssler, J. T.; Matzger, A. J. FT Raman and DFT Study on a Series of All-anti Oligothienoacenes End-Capped with Triisopropylsilyl Groups. *ChemPhysChem* **2009**, *10*, 3069−3076.
(33) Sokolov, A. N.; Atahan-Evrenk, S.; Mondal, R.; Akkerman, H. B.; Sánchez-Carrera, R. S.; Granados-Focil, S.; Schrier, J.; Mannsfeld, S. C. B.; Zoombelt, A. P.; Bao, Z.; Aspuru-Guzik, A. From computational discovery to experimental characterization of a high hole mobility organic crystal. *Nat. Commun.* **2011**, *2*, 437.
(34) Yao, Y.; Dong, H.; Hu, W. Charge Transport in Organic and Polymeric Semiconductors for Flexible and Stretchable Devices. *Adv. Mater.* **2016**, *28*, 4513−4523.
(35) Kim, Y. C.; Jeon, N. J.; Noh, J. H.; Yang, W. S.; Seo, J.; Yun, J. S.; Ho-Baillie, A.; Huang, S.; Green, M. A.; Seidel, J.; Ahn, T. K.; Seok, S. I. Beneficial Effects of $PbI_2$ Incorporated in Organo-Lead Halide Perovskite Solar Cells. *Adv. Energy Mater.* **2016**, *6*, 1502104.
(36) Jeon, N. J.; Noh, J. H.; Yang, W. S.; Kim, Y. C.; Ryu, S.; Seo, J.; Seok, S. I. Compositional engineering of perovskite materials for high-performance solar cells. *Nature* **2015**, *517*, 476−80.


DOI: 10.1021/acs.chemmater.8b04003
*Chem. Mater.* XXXX, XXX, XXX−XXX